

# Relaxation Effects in Small Critical Nozzles

Aaron N. Johnson  
e-mail: aaron.johnson@nist.gov

Charles L. Merkle

Michael R. Moldover

John D. Wright

National Institute of Standards and Technology,  
100 Bureau Drive, Stop 8361,  
Gaithersburg, Maryland, 20899-8361

We computed the flow of four gases (He, N<sub>2</sub>, CO<sub>2</sub>, and SF<sub>6</sub>) through a critical flow venturi (CFV) by augmenting traditional computational fluid dynamics (CFD) with a rate equation that accounts for  $\tau_{\text{relax}}$ , a species-dependent relaxation time that characterizes the equilibration of the vibrational degrees of freedom with the translational and rotational degrees of freedom. Conventional CFD ( $\tau_{\text{relax}}=0$ ) underpredicts the flow through small CFVs (throat diameter  $d=0.593$  mm) by up to 2.3% for CO<sub>2</sub> and by up to 1.2% for SF<sub>6</sub>. When we used values of  $\tau_{\text{relax}}$  from the acoustics literature, the augmented CFD underpredicted the flow for SF<sub>6</sub> by only 0.3%, in the worst case. The augmented predictions for CO<sub>2</sub> were within the scatter of previously published experimental data ( $\pm 0.1\%$ ). As expected, both conventional and augmented CFD agree with experiments for He and N<sub>2</sub>. Thus, augmented CFD enables one to calibrate a small CFV with one gas (e.g., N<sub>2</sub>) and to use these results as a flow standard with other gases (e.g., CO<sub>2</sub>) for which reliable values of  $\tau_{\text{relax}}$  and the relaxing heat capacity are available. [DOI: 10.1115/1.2137346]

## 1 Introduction

Critical flow venturis (CFVs), also called critical nozzles, have been used for decades as secondary standards for measuring large gas flows because they are passive, extraordinarily stable, and easy to use [1,2]. In an effort to exploit these desirable qualities at the lower flow ranges encountered in semiconductor processing (10 to 300 standard<sup>1</sup> cm<sup>3</sup> s<sup>-1</sup>), we used computational fluid dynamics (CFD) to predict the flow through a small, well-characterized CFV (nominal throat diameter  $d=0.593$  mm).<sup>2</sup> In Fig. 1, we compare our CFD results with previously published measurements for four gases [3]. The variables used for this comparison are those conventionally used to describe CFVs. Thus, the ordinate is the discharge coefficient  $C_d \equiv \dot{m}/\dot{m}_i$ , where  $\dot{m}$  is actual mass flow and  $\dot{m}_i$  is the mass flow calculated using an idealized one-dimensional, inviscid model. The abscissa is the inverse square root of the Reynolds number:  $\text{Re} = 4\dot{m}_i/\pi d\mu_o$  where  $\mu_o$  is the viscosity evaluated upstream of the CFV at stagnation conditions. As shown in Fig. 1, the present CFD model predicts the mass flow through the small CFV for all four gases to within  $\pm 0.31\%$  for flow rates spanning at least a factor of 4 for each gas. Previously existing CFD models and analytical predictions [4–11] account for several species-dependent effects (virial coefficients and temperature-dependent heat capacity) and for boundary layers and curvature of the sonic line. In order to obtain good agreement with the measurements for CO<sub>2</sub> and SF<sub>6</sub>, we had to augment existing equilibrium CFD models to account for  $\tau_{\text{relax}}$ , the species-dependent relaxation time that characterizes the equilibration of the vibrational degrees of freedom with the translational and rotational degrees of freedom. The relaxation time must be compared to  $\tau_{\text{transit}}$ , the average time required for a fluid element of fixed mass to move from the CFV inlet to the CFV throat. For any ISO standardized CFV geometry [12] (Fig. 2), the approximate transit time is  $\tau_{\text{transit}} \approx 10d/c$  where  $d$  is the diameter of the throat and  $c$  is the speed of sound in the gas at the CFV throat. Thus, small CFVs, such as the one considered here for use at low flow rates, have short transit times and can encounter larger values of the ratio  $\Gamma = \tau_{\text{relax}}/\tau_{\text{transit}}$ . Conventional CFD and analytical theo-

ries for CFVs assume  $\tau_{\text{relax}}=0$ . Such theories agree with the present results for N<sub>2</sub> and He within their scatter (0.1%, root mean square); however, as shown in the lower panel of Fig. 1, conventional theories ( $\tau_{\text{relax}}=0$ ) underpredict the flow through this small CFV by up to 2.3% for CO<sub>2</sub> and up to 1.2% for SF<sub>6</sub>. The augmented CFD model provides better understanding of how gas species effects influence the discharge coefficient for both CO<sub>2</sub> and SF<sub>6</sub> in small CFVs. The results help to quantify the level of correction needed when a CFV is calibrated using a standard gas (e.g., N<sub>2</sub> or air, Ar, etc.) where  $\tau_{\text{relax}}=0$ , but applied to other gases (e.g., CO<sub>2</sub> or SF<sub>6</sub>) where vibrational relaxation effects are prevalent.

Our CFD model characterizes the vibrational degrees of freedom within each fluid element by its energy  $\epsilon_{\text{vib}}(T_{\text{vib}})$ , where  $T_{\text{vib}}$  is the vibrational temperature. As the gas flows through the CFV, the temperature of the external modes,  $T_{\text{ext}}$ , drops quickly while  $T_{\text{vib}}$  lags behind for molecules where  $\Gamma$  is close to or greater than unity. (Here, we follow Bhatia [13] who called the translational and rotational degrees of freedom “external modes.”) To account for the lag, our CFD model couples the Navier-Stokes equations to a local relaxation equation that contains two species-dependent parameters. One is  $\epsilon_{\text{vib}}(T_{\text{vib}})$  which is obtained from spectroscopy [13,14] and the second is  $\tau_{\text{relax}}$  which is obtained from ultrasonic absorption and dispersion data [15,16]. The CFD flow field is determined by solving the coupled equations simultaneously.

Our results show that relaxation effects must be considered whenever small CFVs are used for slowly relaxing gases over temperatures ranges for which the vibrational states are significantly populated. Both CO<sub>2</sub> and SF<sub>6</sub> meet these conditions; however, N<sub>2</sub> does not because, at ambient temperature, nearly all N<sub>2</sub> molecules are in their lowest vibrational state.

## 2 CFV Geometry and Principle of Operation

**2.1 CFV Geometry.** Figure 2 shows the contour of an ISO toroidal throat CFV that was used in this study. It consists of a circular arc of radius  $R_c=2d$  that merges smoothly into a conical section with a vertex half-angle of  $\theta=3^\circ$ .

**2.2 Baseline Mass Flow Model.** For any CFV, the ratio of the downstream pressure to upstream pressure is maintained so that the gas velocity near the CFV throat reaches sonic velocity. This condition is commonly referred to as choking the CFV. The largest pressure ratio that just chokes the CFV is called the choking pressure ratio, and CFVs must be operated at or below this thresh-

<sup>1</sup>Standard reference conditions are at 293.15 K and 101.325 kPa.

<sup>2</sup>The measured value of the throat diameter was adjusted by less than one micron by matching the experimental  $C_d$  data to the computed results for N<sub>2</sub>.

Contributed by the Fluids Engineering Division of ASME for publication in the JOURNAL OF FLUIDS ENGINEERING. Manuscript received July 10, 2003; final manuscript received August 10, 2005. Review conducted by Joseph Katz.

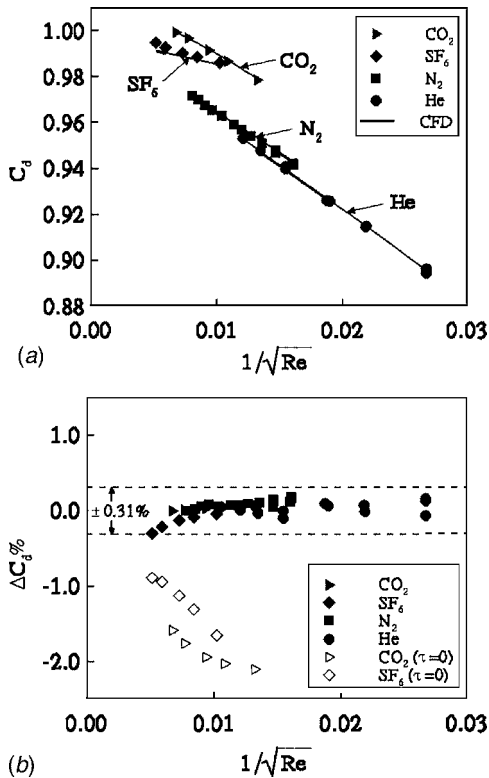


Fig. 1 Comparison of experimental calibration data of four gases with equilibrium (open symbols in (b)) and nonequilibrium CFD data (closed symbols) over a Reynolds number range from 2000 to 40,000

old. For choked conditions, a long standing *baseline* mass flow model has been developed that is capable of predicting the actual mass flow to within 10% or better, depending on Reynolds number. This model is based on the following three assumptions: (1) the flow field is one-dimensional, (2) the flow field is inviscid, and (3) the gas behaves ideally and has constant heat capacities. Herein, these assumptions are collectively called the *baseline CFV assumption*. Several engineering texts [17–19] use this assumption to derive a baseline mass flow

$$\dot{m}_i = \frac{P_o A^* C_s^i}{\sqrt{RT_o}} \quad (1)$$

where  $P_o$  is the upstream stagnation pressure,  $T_o$  is the upstream stagnation temperature,  $A^* = \pi d^2/4$  is the CFV throat area,  $R$  is the gas constant for a given species (the universal gas constant divided by the molecular weight), and  $C_s^i$  is the ideal critical flow function

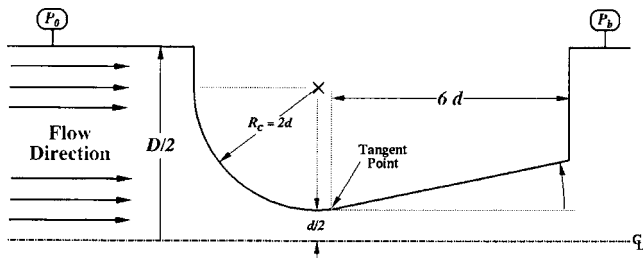


Fig. 2 Critical nozzle used in this study. The diameter of the throat was  $d=0.593$  mm.

$$C_s^i = \sqrt{\gamma} \left( \frac{\gamma+1}{2} \right)^{(1+\gamma/2(1-\gamma))} \quad (2)$$

where the superscript “i” is added to denote the gas is ideal and  $\gamma = C_p/C_v$  is the ratio of the constant-pressure specific heat to the constant-volume specific heat.

**2.3 Experimental Calibration.** In CFV applications, none of the three assumptions used to derive the baseline mass flow are perfectly satisfied, and consequently the actual CFV mass flow does not equal  $\dot{m}_i$ . However, the baseline mass flow plays a vital role in CFV calibrations, being used as the normalizing parameter in the definition of the discharge coefficient

$$C_d \equiv \frac{\dot{m}}{m_i} = \frac{\dot{m} \sqrt{RT_o}}{P_o A^* C_s^i} \quad (3)$$

where  $\dot{m}$  is the experimentally measured mass flow. Calibration curves typically plot the discharge coefficient versus a function of the Reynolds number

$$Re = \frac{4\dot{m}_i}{\pi d \mu_o} \quad (4)$$

where  $\mu_o$  is the molecular viscosity evaluated at the stagnation conditions.

The  $C_d$  values resulting from experimental calibration curves are most reliable when they are applied using the same conditions (i.e., gas species, stagnation conditions, ambient temperature, inlet velocity profile, beta ratio, etc.) for which the CFV was calibrated. This paper focuses on how species effects impact the discharge coefficient when the calibration and application gas differ and one or both of these gases experiences vibrational relaxation. It is important to understand this phenomenon because this physical mechanism is not captured by the standard Reynolds number parameterization. In a similar manner, species effects attributed to real gas behavior (i.e., virial effects) also result in uncoupling between the discharge coefficient and Reynolds number. While the physical mechanisms differ, we introduce linear CFV theory and use it to show that the methodology used to account for real gas behavior can also be applied to correct for vibrational relaxation phenomenon.

In CFV flows, real gas behavior is taken into account by using the real gas critical flow function,  $C_s^r$ , in the place of the ideal critical flow function,  $C_s^i$ , in Eq. (3). When real gas behavior is accounted for in this way, the corresponding discharge coefficient depends predominantly on Reynolds number.<sup>3</sup> In a similar manner, we introduce an *effective* critical flow function,  $C_s^{eff}$ , to correct for vibrational relaxation effects. The effectiveness of this correction parameter, like the correction for real gas behavior, depends on vibrational relaxation phenomena being uncoupled from the other higher order effects (i.e., boundary layer development, the shape of the sonic line, and virial effects). Higher order CFV models, which correct the baseline mass flow model, can be used to justify the use of this correction factor.

**2.4 Higher Order CFV Models.** Higher order CFV models improve upon the baseline mass flow model by eliminating the three assumptions used to derive  $\dot{m}_i$ . These higher order models are based on solutions of the Navier-Stokes equations that govern the fluid dynamics of conventional CFV flows. Because of the complexity of the Navier-Stokes equations, no analytical solutions have been found when all three of the baseline CFV assumptions are eliminated simultaneously. Instead, researchers have found three different solutions by removing only one of the three baseline CFV assumptions while enforcing the other two. These three solutions include (1) a solution to account for the boundary layer

<sup>3</sup>Even after correcting for real gas behavior the discharge coefficient has a weak dependence on  $\gamma$  that diminishes with increasing Reynolds number.

development along the CFV wall [6–8], (2) an inviscid axisymmetric solution to account for the curvature of the sonic line at the CFV throat [4], and (3) a solution to account for real gas behavior [20–24]. We briefly discuss each of these three solutions.

In the late 1960s and early 1970s both Tang [6,7] and Geropp [8] independently developed models predicting how the discharge coefficient is affected by boundary layer development along the CFV wall. The viscous discharge coefficient developed by these researchers

$$C_{d1} = f_1(\text{Re}, \gamma, \Omega) \quad (5)$$

is denoted by the subscript “1” and is a function of the Reynolds number, the specific heat ratio, and the CFV geometry which is accounted for via the curvature parameter  $\Omega = d/2r_c$  where  $r_c$  is the throat radius of curvature.

The second model, developed by Hall in 1962, predicts the effects of sonic line curvature on the discharge coefficient. Hall eliminated the one-dimensional assumption by considering the flow to be axisymmetric, but he retained the assumptions that the fluid behaves as a perfect gas and the flow is inviscid. The axisymmetric inviscid discharge coefficient

$$C_{d2} = f_2(\gamma, \Omega) \quad (6)$$

is denoted by the subscript “2” and is a function of the specific heat ratio and the curvature parameter. The third model was developed by Johnson [20–24] who included real gas behavior, but assumed that the flow was inviscid and one-dimensional. This solution requires an accurate thermodynamic database and is typically implemented numerically as described in Refs. [20–24]. For convenience, Johnson expressed the numerically calculated mass flow in the same format as the baseline model

$$\dot{m}_3 = \frac{P_o A^* C_s^r}{\sqrt{RT_o}} \quad (7)$$

and lumped all of the real gas effects into the parameter  $C_s^r$ , which replaces the ideal critical flow function. The real discharge coefficient is denoted by the subscript “3” and is defined as the ratio of  $\dot{m}_3$  and the baseline mass flow

$$C_{d3} \equiv \frac{\dot{m}_3}{\dot{m}_1} = \frac{C_s^r}{C_s^i} \quad (8)$$

but by Eqs. (1) and (7) is also equal to the ratio of the real gas critical flow function to the ideal critical flow function. The real gas critical flow function, which is often called the *Johnson coefficient*, is generally either tabulated as a function of  $P_o$  and  $T_o$  or given as a surface fit of these parameters for various gas species.

**2.5 Linear CFV Theory.** For simplicity, in this paper, the three CFV models are referred to as models 1, 2, and 3, respectively. Linear CFV theory is used to combine the individual results of these three models into a single model capable of predicting the discharge coefficient for a general CFV flow where none of the baseline CFV assumptions apply. The results of the linear theory [11] show that to second-order accuracy the discharge coefficient equals

$$C_d = C_{d1} C_{d2} C_{d3} \quad (9)$$

the product of the  $C_{di}$ 's from models 1, 2, and 3, respectively. This expression clearly shows how the discharge coefficient depends on real gas behavior via  $C_{d3}$ . This dependence can be eliminated by dividing Eq. (9) by  $C_{d3}$ , and modifying the discharge coefficient definition to be

$$C'_d \equiv C_d / C_{d3} = C_{d1} C_{d2} \quad (10)$$

Based on the functionality of  $C_{d1}$  and  $C_{d2}$  given in Eqs. (5) and (6) the modified discharge coefficient is completely free of virial effects, being a function of  $\text{Re}$ ,  $\gamma$ , and  $\Omega$ . Physically,  $C'_d$  is made

independent of real gas behavior by using  $\dot{m}_3$  as the normalizing parameter

$$C'_d \equiv \frac{\dot{m}}{\dot{m}_3} = \frac{\dot{m} \sqrt{RT_o}}{P_o A^* C_s^i}, \quad (11)$$

which is equivalent to using the real gas critical flow function in place of the ideal critical flow function. Mathematically, Eq. (11) is derived by substituting Eqs. (3) and (8) into Eq. (10).

The definition of the discharge coefficient given in Eq. (11) is preferred over the definition in Eq. (3) because the real gas behavior in Eq. (3) has the undesired quality of possibly permitting the discharge coefficient to be greater than unity. That is, depending on the gas and CFV operating conditions,  $C_{d3}$  could either be greater than or less than unity. In cases where  $C_{d3} > 1$ , it could cause the discharge coefficient in Eq. (3) to be greater than unity. On the other hand, the definition in Eq. (11) is only dependent on boundary layer effects and curvature of the sonic line as shown in Eq. (10). Both of these effects cause the discharge coefficient to be less than unity. The boundary layer introduces a region of fluid where both the density and velocity are reduced relative to the core flow. The density is lower because of the higher temperatures in the boundary layer attributed to viscous heating as the flow stagnates at the CFV wall, and the fluid velocity is lower due to the no-slip condition imposed by the wall. In the axisymmetric core flow, the curvature of the sonic line stipulates that the Mach number distribution across the CFV throat cross section is not uniformly equal to unity, but has values both below and above this value. Since compressible flow theory requires that the maximum mass flux coincide with a unity mach number [17], the predicted mass flow will be lower than  $\dot{m}_i$ .

### 3 Methodology

In this section, we present the Navier-Stokes equations that are solved in a conventional equilibrium CFD analysis [9]. We then introduce the extensions required to account for molecular relaxation and we conclude with a description of the numerical algorithms that we used.

**3.1 Conventional CFD Equations.** For Reynolds numbers below  $10^6$ , the axisymmetric, steady, compressible flow in a CFV is governed by the laminar Navier-Stokes equations [9]. The large favorable pressure gradient in the converging section of the CFV is believed to relaminarize what would otherwise be a turbulent flow [25]. Evidence that the flow is laminar is observed in myriads of calibration data where, as predicted by laminar flow theory, the discharge coefficient scales linearly with the inverse square root of the Reynolds number (e.g., Fig. 1).

In CFD, the four scalar conservation equations, including continuity, axial and radial momentum, and energy that constitute the axisymmetric Navier-Stokes equations, are often combined into a single vector equation as explained in Refs. [26,27]. In the present numerical investigation the vector form of the Navier-Stokes equations is expressed as

$$Y \frac{\partial Q_v}{\partial t} + \frac{\partial E}{\partial x} + \frac{\partial F}{\partial r} = H + \zeta(Q_v) \quad (12)$$

where the time derivative is retained to facilitate a time marching numerical procedure to the desired steady-state solution.<sup>4</sup> This vector representation of the Navier-Stokes equations is developed by grouping the appropriate variables from the four scalar conservation equations. In particular, those variables having like derivative operators are combined into vectors. For example, the time derivative vector,  $Q_c = [\rho, \rho u_x, \rho u_r, e]^T$ , consists of the temporal terms from continuity, axial and radial momentum, and energy equations where  $e = \rho[\varepsilon + 1/2(u_x^2 + u_r^2)]$  is the sum of the internal

<sup>4</sup>The time marching approach differs from commonly used iterative approaches which omit the time derivative term when applied to steady state problems.

and kinetic energy per unit volume. In Eq. (12) the time derivative is multiplied by the Jacobian matrix,  $Y = \partial Q_c / \partial Q_v$ , so that via the chain rule of vector calculus [28],  $Q_c = [\rho, \rho u_x, \rho u_r, e]^T$ , is replaced by  $Q_v = [P, u_x, u_r, T]^T$ . This transformation to the dependent vector,  $Q_v$ , conveniently allows thermodynamic properties to be evaluated explicitly as a function of temperature and pressure in the numerical procedure.

The remaining vectors,  $E$  and  $F$ , on the left-hand side of Eq. (12) are determined in a manner analogously to  $Q_c$ . These vectors, commonly called the inviscid flux vectors, are defined as

$$E = \begin{bmatrix} \rho u_x \\ \rho u_x^2 + P \\ \rho u_x u_r \\ (e + P) u_x \end{bmatrix}, \quad F = \begin{bmatrix} \rho u_r \\ \rho u_r u_x \\ \rho u_r^2 + P \\ (e + P) u_r \end{bmatrix} \quad (13)$$

and account for the convective terms in the mass, momentum, and energy equations. On the right-hand side of Eq. (12), the viscous operator,  $\zeta$ , is defined by

$$\zeta = \frac{\partial}{\partial x} \left( R_{xx} - \frac{\partial}{\partial x} \right) + \frac{\partial}{\partial x} \left( R_{xr} \frac{\partial}{\partial r} \right) + \frac{\partial}{\partial r} \left( R_{rx} \frac{\partial}{\partial x} \right) + \frac{\partial}{\partial r} \left( R_{rr} \frac{\partial}{\partial r} \right) \quad (14)$$

where the viscous matrices,  $R_{xx}$ , and  $R_{xr}$  are given by

$$R_{xx} = \begin{bmatrix} 0 & 0 & 0 & 0 \\ 0 & \frac{4}{3}\mu & 0 & 0 \\ 0 & 0 & \mu & 0 \\ 0 & \frac{4}{3}\mu u_x & \mu u_r & \kappa \end{bmatrix}, \quad R_{xr} = \begin{bmatrix} 0 & 0 & 0 & 0 \\ 0 & 0 & -\frac{2}{3}\mu & 0 \\ 0 & \mu & 0 & 0 \\ 0 & \mu u_r & -\frac{2}{3}\mu u_r & 0 \end{bmatrix} \quad (15)$$

with  $R_{rx}$  and  $R_{rr}$  having analogous forms. Finally, the vector  $H$  contains the axisymmetric source terms as given in Ref. [27].

### 3.2 Thermodynamic and Nonequilibrium Considerations.

We follow conventional CFD for dilute gases by computing the density from the equation of state,  $\rho = P/[RT(1+B\rho)]$ , where the second virial coefficient  $B(T)$  accounts for real gas behavior. Data for the second virial coefficient and its temperature derivatives were obtained from Refs. [29,30]. We used the transport property data as a function of temperature (at  $P = 101.325$  kPa) from Refs. [31,32]. In conventional CFD, the equilibrium internal energy  $\epsilon^{eq}(\rho, T)$  is calculated from a reference state by integrating the ideal-gas constant-volume specific heat  $C_{v_i}$  and subtracting a correction term to account for real gas effects

$$\epsilon^{eq}(\rho, T) = \int_{T_{ref}}^T C_{v_i} dT - R\rho T^2 \frac{dB}{dT} \quad (16)$$

This formula for  $\epsilon^{eq}(\rho, T)$  is unsatisfactory for the CFV in Fig. 2 for certain gases. For this CFV,  $\tau_{transit} \approx 20 \mu s$ . Vibrational relaxation times range from 0.0001 to 10  $\mu s$  depending on gas species, temperature, and density. Thus, the conventional CFD assumption  $\Gamma = \tau_{relax} / \tau_{transit} = 0$  is a poor approximation for gases with slowly relaxing vibrational modes, especially near the throat of the CFV where the acceleration of the gas is largest. The increase in kinetic energy near the CFV throat is balanced by a decrease in the internal energy of the translational and rotational modes. This reduces the temperature  $T_{ext}$  that characterizes these modes. Because the vibrational modes relax slowly, the temperature characterizing them,  $T_{vib}$ , is significantly higher than  $T_{ext}$ . Consequently, the value of internal energy is not accurately predicted by Eq. (16).

To accurately predict the internal energy when  $T_{vib} \neq T_{ext}$ , we

sum the relevant molecular components including contributions from translational, rotational, and vibrational modes<sup>5</sup>

$$\epsilon(\rho, T_{vib}, T_{ext}) \equiv \epsilon_{ext}(\rho, T_{ext}) + \epsilon_{vib}(T_{vib}) \quad (17)$$

The second term,  $\epsilon_{vib}(T_{vib})$ , accounts for the vibrational modes. We assume that the vibrational modes are always in internal equilibrium with each other and we compute  $\epsilon_{vib}(T_{vib})$  by summing the contribution of each vibrational mode

$$\epsilon_{vib}(T_{vib}) = \sum_{n=1}^N \frac{g_n R \theta_n}{\exp(\theta_n / T_{vib}) - 1} \quad (18)$$

where  $g_n$  is the degeneracy for the  $n$ th vibrational mode,  $\theta_n$  is the characteristic vibrational temperature for the  $n$ th mode, and  $N$  is the number of active vibrational modes [13,14]. The first term in Eq. (17),  $\epsilon_{ext}(\rho, T_{ext})$ , is called the *external molecular energy*, which consists of both the translational and rotational molecular components. Both of these components are taken to be fully equilibrated so that  $T_{ext}$  equals the thermodynamic temperature  $T$ . The external molecular energy can be defined by subtracting the equilibrium vibrational energy from the equilibrium internal energy

$$\epsilon_{ext}(\rho, T_{ext}) = \epsilon^{eq}(\rho, T_{ext}) - \epsilon_{vib}(T_{ext}). \quad (19)$$

In this way  $\epsilon_{ext}(\rho, T_{ext})$  consists only of the translational and rotational components, yet retains real gas behavior that traditional ideal gas models of the translational and rotational components omit.

The exchange of energy between vibrational modes and the combined translational and rotational modes was modeled using the vibrational rate equation [13]

$$\frac{D\epsilon_{vib}(T_{vib})}{Dt} = \frac{\epsilon_{vib}(T_{ext}) - \epsilon_{vib}(T_{vib})}{\tau_{relax}} \quad (20)$$

where  $D/Dt$  is the time derivative following a fluid element of fixed mass. Bhatia developed this equation for diatomic molecules having only a single vibrational degree of freedom and therefore only one relaxation time [13]. However, Eq. (20) works well for polyatomic molecules at temperatures low enough so that only the lowest vibrational degree of freedom is active (e.g.,  $CO_2$  near ambient temperature). Often Eq. (20) is used to model relaxation in sound and shock propagation through polyatomic gases, such as  $SF_6$ , where the highest vibrational modes relax quickly so that the entire heat capacity relaxes at a single relaxation time. However, for certain polyatomic gases (e.g.,  $C_2H_6$ ) more than one relaxation time is needed as discussed by Lambert [33].

For steady flow along a streamline the vibrational rate equation is given by

$$\Gamma \frac{d\epsilon_{vib}(T_{vib})}{dz} = \epsilon_{vib}(T_{ext}) - \epsilon_{vib}(T_{vib}) \quad (21)$$

where  $\Gamma = \tau_{relax} / \tau_{transit}$  is the ratio of the local relaxation time to the local flow transit time, and  $z = s/L$  is the normalized distance along a streamline **where  $s$  is the distance along a streamline starting at the CFV entrance, and  $L$  is the total distance along the streamline**. Here,  $\tau_{transit} = L/|\vec{u}|$  is the time that it takes for a fluid particle to move a distance  $L$  along a streamline, and  $|\vec{u}|$  is the magnitude of average velocity over that distance. The relaxation time changes with the local thermodynamic conditions according to the phenomenological Landau and Teller relation [34]

<sup>5</sup>The contribution of the electronic energy is negligible over the temperature range of interest.

$$\tau_{\text{relax}} = \frac{K_1 \exp[(K_2/T_{\text{ext}})^{1/3}]}{P} \quad (22)$$

where the constants  $K_1$  and  $K_2$  were obtained by fitting ultrasonic relaxation data [15,16].

**3.3 Numerical Solution.** The vibrational rate equation and the Navier-Stokes equations must be solved as a coupled system of equations. In this work these equations are solved by globally iterating between the Navier-Stokes equations and the vibrational rate equation until both are simultaneously satisfied. The iterative procedure begins by solving the Navier-Stokes equations with a guessed value of the molecular vibrational energy,  $\varepsilon_{\text{vib}}(T_{\text{vib}})$ . From the latest solution of the Navier-Stokes, the input parameters,  $\Gamma = \tau_{\text{relax}}/\tau_{\text{transit}}$  and  $\varepsilon_{\text{vib}}(T_{\text{ext}})$ , are determined for the vibrational rate equation. Next, the vibrational rate equation is integrated along streamlines to determine the updated vibrational energy,  $\varepsilon_{\text{vib}}(T_{\text{vib}})$ , which is used to determine the modified internal energy,  $\varepsilon(\rho, T_{\text{vib}}, T_{\text{ext}})$ , in the next iteration of the Navier-Stokes equations. Consequently, the Navier-Stokes solution and the vibrational rate solution are co-dependent.

**3.4 Numerical Solution of the Navier-Stokes Equations.** The Navier-Stokes equations are solved in a conventional body-fitted coordinate system [35] with a physical domain equivalent to the CFV geometry shown in Fig. 2. Grid-independent solutions are obtained using a mesh with 201 axial grid points and 101 radial grid points. The axial grid points are uniformly spaced while the radial grid points are spaced exponentially with a higher grid density near the CFV wall to resolve the boundary layer.

An alternating-direction implicit (ADI) numerical algorithm [26,27] is used for integrating the Navier-Stokes equations. Time advancement is obtained using first-order, backward finite differences. Both inviscid and viscous time-derivative preconditioning [36–38] are employed for accelerated convergence rates over a wide range of Mach numbers and Reynolds numbers. Spatial discretization is accomplished using third-order up-winded flux differences for the convective terms and central differences for the diffusive terms. The resulting numerical scheme consists of two tridiagonal matrices that are inverted at each time step using a block version of the Thomas algorithm [26,27].

In these computations boundary conditions are specified at the CFV inlet, at the CFV exit, along the CFV wall, and on the centerline. At the inlet, the stagnation pressure, stagnation temperature, and flow angle are specified. Characteristic boundary conditions [39] are specified at the supersonic CFV exit. On the CFV centerline, symmetry boundary conditions are used. The CFV wall is taken to be adiabatic with a zero normal pressure gradient and a no-slip velocity boundary condition.

**3.5 Numerical Solution of the Vibrational Rate Equation.** In contrast to the Navier-Stokes equations, which are expressed in a Eulerian sense, the vibrational rate equation is expressed in a Lagrangian sense. Specifically, the vibrational rate equation describes the rate of relaxation of the vibrational modes of a gas particle of fixed identity moving through the flow field. The Lagrangian paths of particles of fixed identity correspond to streamlines in the flow field. The trajectories of these streamlines must be estimated from the Navier-Stokes solution before the vibrational rate equation can be solved. In the coupling procedure between the two equation sets, the streamlines in the flow field are computed after each time step using the most recent approximation to the Navier-Stokes solution. The vibrational rate equation is then solved on each streamline by a space-marching procedure that integrates between consecutive points on a streamline.

The space-marching procedure begins at the CFV inlet where the vibrational energy on each streamline is equal to its equilibrium value. To find the value of the vibrational energy,  $\varepsilon_{\text{vib}}(T_{\text{vib}})$ , at the next adjacent grid point along the stream line, the vibrational rate equation is analytically integrated using variation of

parameters [40]. In turn, this value of  $\varepsilon_{\text{vib}}(T_{\text{vib}})$  serves as an initial condition for the next point, and so on, until the complete streamline has been updated. This process is then repeated for each streamline in the flow field.

## 4 Results

**4.1 Validation of CFD Model.** The CFD methodology followed the procedure used for the experimental calibration, where the mass flow was controlled by varying the stagnation pressures in the range  $50 \text{ kPa} < P_o < 200 \text{ kPa}$  while maintaining the stagnation temperature at 298.15 K. For these operating conditions, the corresponding Reynolds number varied from 1000 to 40,000 for the small throat ISO standardized CFV. The CFD results were verified by comparisons with experimental data for four gases including He,  $\text{N}_2$ ,  $\text{SF}_6$ , and  $\text{CO}_2$ .

The experimental data shown in Fig. 1 were obtained by Japan's national flow standard, which measures flow using a gravimetric timed-collection technique with an uncertainty of 0.1% [3]. As shown in Fig. 1, the nonequilibrium CFD model predicted the discharge coefficient to better than 0.3% for all of the gases over the entire Reynolds number range. In agreement with experimental results, the nonequilibrium CFD model predicted larger  $C_d$  values for  $\text{SF}_6$  and  $\text{CO}_2$ —gases affected by relaxation. As expected, the nonequilibrium CFD model correctly predicted  $C_d$  for He and  $\text{N}_2$ , gases that are not influenced by vibrational non-equilibrium.

**4.2 Increase in  $C_d$  due to Vibrational Nonequilibrium Flow.** When slowly relaxing gases are used in small CFVs, the measured mass flow exceeds the predicted value given by models that assume  $\tau_{\text{relax}}=0$ . Indeed, the discharge coefficient as defined in Eq. (3) or (11) may even be greater than unity. To understand this phenomenon, it is helpful to consider the limiting cases for the ratio  $\Gamma = \tau_{\text{relax}}/\tau_{\text{transit}}$ . The limit  $\Gamma \rightarrow 0$  is the case of equilibrium flow; the limit  $\Gamma \rightarrow \infty$  is “frozen” flow in which energy in vibrational modes remains constant. In both limiting cases, the gas dynamic equations are uncoupled from the vibrational rate equation.

In the limit of frozen flow, relaxation does not occur or, equivalently  $\varepsilon_{\text{vib}}(T_{\text{vib}}) = \varepsilon_{\text{vib}}(T_o) = \text{const}$  throughout the flow field. Because  $\varepsilon_{\text{vib}}(T_o)$  is constant, the frozen flow heat capacity of the vibrational degrees of freedom is zero ( $C_{V_{\text{vib}}} = 0$ ). Consequently, the specific heat ratio for frozen flow,  $\gamma^{\text{fr}}$ , is larger than the equilibrium value,  $\gamma^{\text{eq}}$ . The ideal gas model can be used to demonstrate this fact. For an ideal gas, the specific heat ratio is expressible in terms of the translational, rotational, and vibrational heat capacities [18]

$$\gamma_{\text{ideal}} = 1 + \frac{R}{C_{V_{\text{trans}}} + C_{V_{\text{rot}}} + C_{V_{\text{vib}}}} \quad (23)$$

where  $\gamma^{\text{fr}}$  is calculated by setting  $C_{V_{\text{vib}}} = 0$ . For diatomic or polyatomic gases, having a least one active vibrational mode,  $C_{V_{\text{vib}}} > 0$  so that  $\gamma^{\text{fr}} > \gamma^{\text{eq}}$ .

The increased value of the specific heat ratio in the case of frozen flow results in a higher sound speed in the gas than would exist for equilibrium flow. In addition, as the gas expands and accelerates through the CFV it cools to a lower temperature in the case of frozen flow than it would for equilibrium flow. This lower temperature subsequently results in a higher density. Both the higher speed of sound and the higher density, in the case of frozen flow, increase the mass flow through the CFV as shown by combining Eqs. (1) and (2) using the larger frozen flow specific heat ratio in place of normal value of  $\gamma$ . Finally, in the intermediate case of vibrational relaxation, previous CFD results have shown that the mass flow is increased above the equilibrium value, but is less than the frozen flow value [10].

When vibrational relaxation is present, the discharge coefficient as defined by either Eq. (3) or (11) is higher than would be pre-

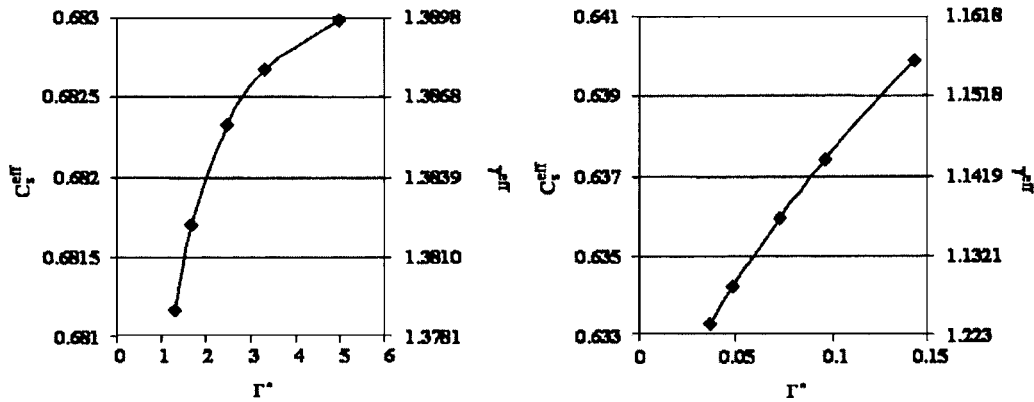


Fig. 3 Effective critical flow function versus reference value of  $\Gamma^*$  evaluated at the nozzle throat for CO<sub>2</sub> (left) and SF<sub>6</sub> (right)

dicted by conventional equilibrium models. The larger discharge coefficient results because the normalizing parameter  $\dot{m}_i$  or  $\dot{m}_3$  does not account for increased mass flow attributed to vibrational relaxation. Moreover, these definitions allow values of the discharge coefficient that are greater than unity [11]. To avoid this nonphysical situation,<sup>6</sup> the discharge coefficient should be defined using a normalizing parameter that accounts for vibrational relaxation effects.

**4.3 Generalizing the Critical Flow Function to Account for Vibrational Relaxation.** Vibrational relaxation can be accounted for by generalizing the critical flow function, which itself is a generalization of the discharge coefficient. Based on linear CFV theory it can be shown that an *effective* critical flow function can be defined as

$$C_s^{eff} \equiv C_s^r \left( \frac{C_d^{vib}}{C_d^{eq}} \right) \quad (24)$$

where  $C_d^{vib}$  is the discharge coefficient computed with the present vibrational relaxation flow model, and  $C_d^{eq}$  is the discharge coefficient computed with the equilibrium flow model.

Figure 3 shows the *effective* critical flow function for both CO<sub>2</sub> and for SF<sub>6</sub> gases as a function of  $\Gamma^*(T_o, P_o) = \tau_{relax}^* / \tau_{transit}^*$  where  $\tau_{relax}^*$  is evaluated at the throat conditions using Eq. (22) and  $\tau_{transit}^* = d/c^*$  is the time required for a gas particle to travel one CFV throat diameter at the speed of sound,  $c^* = \sqrt{\gamma RT^*}$ . The *effective* critical flow function defined in this way is valid for an ISO standard CFV geometry for  $T_o$  near room temperature. For a given gas,  $C_s^{eff}$  depends not only on  $\Gamma^*$ , but also on  $C_{vib}/C_v = (\gamma^{fr} - \gamma^{eq}) / (\gamma^{fr} - 1)$ , the ratio of the vibrational specific heat to the total constant-volume specific heat. This ratio, which gives an indication of the number of active vibrational modes, is strongly dependent on temperature so that Fig. 3 is only valid for  $T_o$  near room temperature.

The *effective* critical flow function defines an *effective* specific heat ratio according to the relationship

$$C_s^{eff} = \sqrt{\gamma^{eff}} \left( \frac{\gamma^{eff} + 1}{2} \right)^{(1+\gamma^{eff})/(1-\gamma^{eff})} \quad (25)$$

For both gases CO<sub>2</sub> and SF<sub>6</sub> the *effective* specific heat ratio lies between the equilibrium and frozen flow limit and can be used to assess the degree of vibrational relaxation.

By using  $C_s^{eff}$  in the expression for the ideal theoretical mass flow given in Eq. (1), the generalized discharge coefficient ac-

counts for vibrational relaxation. The resulting  $C_d$  curves for CO<sub>2</sub> and SF<sub>6</sub> will then agree with analytical  $C_d$  predictions, having  $C_d$  values that are less than unity and that scale with the Reynolds number and the specific heat ratio.

## Conclusions

A model for flow through CFVs that incorporates the influence of the relaxation time of vibrational degrees of freedom has been presented. The model agrees with experimental measurements of the discharge coefficient for four gas species (including CO<sub>2</sub> and SF<sub>6</sub>) within 0.31% whereas prior models differed from experiments by as much as 2.3%. The new model couples nonequilibrium thermodynamics with the equations of flow. The pertinent quantities are the energy of vibrational modes and the ratio of the vibrational relaxation time to the transit time for the gas to move from the CFV entrance to its throat. The nonequilibrium phenomena causes an increase in mass flow through the CFV that can be explained by the limiting cases of “frozen” and equilibrium flow. Linear CFV theory is introduced and used to define the appropriate form of the *effective* critical flow function necessary to cancel the effects of vibrational relaxation. The *effective* values of the specific heat ratio and the critical flow function, presented herein, allow a user to use calibration data performed with N<sub>2</sub> to calculate the flow of CO<sub>2</sub> or SF<sub>6</sub> through a CFV without utilizing the computational model.

## Acknowledgment

Computational support was provided by the High Performance Systems and Services Division of the Information Technology Laboratory at NIST. In addition, thanks is extended to Nate Briggs for his ideas and support of this work.

## References

- [1] Wright, J. D., 1998, “The Long Term Calibration Stability of Critical Flow Nozzles and Laminar Flowmeters,” NCSL Conference Proceedings, Albuquerque, NM, pp. 443–462.
- [2] Wright, P. H., 1985, “The Application of Sonic Nozzles to the Automated Accuracy Testing of Gas Flow Meters,” Proc. International Conference on Flow Measurement, Australia, pp. 152–156.
- [3] Nakao, S., Hirayama, T., and Takamoto, M., 1997, “Effects of Thermalphysical Properties of Gases on the Discharge Coefficients of the Sonic Venturi Nozzle,” Proceedings of the 1997 ASME Fluids Engineering Division Summer Meeting, Vancouver, British Columbia, Canada, June 22–26.
- [4] Hall, I. M., 1962, “Transonic Flow in Two-Dimensional and Axially-Symmetric Nozzles,” Q. J. Mech. Appl. Math., XV, Pt. 4, pp. 487–508.
- [5] Smith, R. E., and Matz, R. J., 1962, “A Theoretical Method of Determining Discharge Coefficients for Venturis Operating at Critical Flow Conditions,” J. Basic Eng., 19, pp. 434–446.
- [6] Tang, S. P., 1969, “Theoretical Dependence of the Discharge Coefficients of Axisymmetric Nozzles Under Critical Flows,” Technical Report PR-118-PU, Department of Mechanical Engineering, Princeton Univ., Princeton, NJ.
- [7] Tang, S., 1969, “Discharge Coefficients for Critical Flow Nozzles and Their

<sup>6</sup>Greater than unity  $C_d$  values are sometimes caused by inaccurate values of the CFV throat diameter. This is especially true for small-sized CFVs where the throat diameter is more difficult to measure.

- Dependence on Reynolds Numbers,” Ph.D. thesis, Princeton Univ., Princeton, NJ.
- [8] Geropp, D., 1971, “Laminare Grenzschichten In Ebenen Und Rotationssymmetrischen Lavalduesen,” Deutsche Luft-Und Raumfahrt, Forschungsbericht, pp. 71–90.
- [9] Johnson, A. N., Espina, P. I., Mattingly, G. E., Wright, J. D., and Merkle, C. L., 1998, “Numerical Characterization of the Discharge Coefficient in Critical Nozzles,” *Proceedings of the 1998 NCSL Workshop Symposium*, Albuquerque, NM.
- [10] Johnson, A. N., Wright, J. D., Nakao, S., Merkle, C. L., and Moldover, M. R., 2000, “The Effect of Vibrational Relaxation on the Discharge Coefficient of Critical Flow Venturis,” *Flow Meas. Instrum.*, **11**, pp. 315–327.
- [11] Johnson, A. N., 2000, “Numerical Characterization of the Discharge Coefficient in Critical Nozzles,” Ph.D. thesis, The Pennsylvania State University, University Park, PA.
- [12] ISO 9300: (E), 1990, “Measurement of Gas Flow by Means of Critical Flow Venturi Nozzles,” Geneva Switzerland.
- [13] Bhatia, A. B., 1967, *Ultrasonic Absorption: An Introduction to the Theory of Sound Absorption and Dispersion in Gases, Liquids, and Solids*, Oxford University Press, Inc., London.
- [14] O’Connor, L. C., 1954, “Thermal Relaxation of Vibrational States in Sulfur Hexafluoride,” *J. Acoust. Soc. Am.*, **2**(3), pp. 361–364.
- [15] Estrada-Alexanders, A. F., and Trusler, J. P. M., 1999, “Speed of Sound in Carbon Dioxide at Temperatures between (200 and 450) K and Pressures up to 14 MPa,” *J. Chem. Thermodyn.*, **31**(5), pp. 1589–1601.
- [16] Breshears, W. D., and Blair, L. S., 1973, “Vibrational Relaxation in Polyatomic Molecules: SF<sub>6</sub>,” *J. Chem. Phys.*, **59**(11), pp. 5824–5827.
- [17] John, J. E., 1984, *Gas Dynamics*, 2nd ed., Allyn and Bacon, Inc., Boston.
- [18] Anderson, J. D., Jr., 1982, *Modern Compressible Flow with a Historical Perspective*, McGraw-Hill, Inc., New York.
- [19] Shapiro, A. H., 1954, *The Dynamics and Thermodynamics of Compressible Fluid Flow, Vol. II*, The Ronald Press Co., New York.
- [20] Johnson, R. C., 1963, “Calculation of Real-Gas Effects in Flow Through Critical-Flow-Nozzles,” ASME paper no. 63-WA-71.
- [21] Johnson, R. C., 1964, “Calculations of Real-Gas Effects in Flow Through Critical Nozzles,” *J. Basic Eng.*, **1964**, p. 519.
- [22] Johnson, R. C., 1965, “Real-Gas Effects in Critical-Flow-Through Nozzles and Tabulated Thermodynamic Properties,” Nasa Technical Note D-2565, National Aeronautics and Space Administration, Washington, DC.
- [23] Johnson, R. C., 1968, “Real-Gas Effects in Critical Flow Through Nozzles and Thermodynamic Properties of Nitrogen and Helium at Pressures to 300 × 105 Newtons Per Square Meter (Approx. 300 atm),” NASA Technical Note SP-3046, National Aeronautics and Space Administration, Washington, DC.
- [24] Johnson, R. C., 1971, “Real Gas Effects in Flowmetering,” Symposium on Flow, ISA, Pittsburgh, PA.
- [25] White, F. M., 1991, *Viscous Fluid Flow*, McGraw-Hill Inc., New York.
- [26] Hirsch, C., 1988, *Numerical Computation of Internal and External Flows: Volume 1, Fundamentals of Numerical Discretization*, John Wiley & Sons, Inc., New York.
- [27] Hirsch, C., 1990, *Numerical Computation of Internal and External Flows: Volume 2, Computational Methods for Inviscid and Viscous Flows*, John Wiley & Sons, Inc., New York.
- [28] Davis, D. F., and Snider, A. D., 1991, *Introduction to Vector Analysis, Sixth Edition*, Wm. C. Brown Publishers, Dubuque, IA.
- [29] Hilsenrath, J., Beckett, C. W., Benedict, W. S., Fano, L., Hoge, H. J., Masi, J. F., Nuttall, R. L., Touloukian, Y. S., and Wooley, H. W., 1955, “Tables of Thermal Properties of Gases,” U.S. Department of Commerce NBS Circular 564.
- [30] McCarty, R. D., and Arp, V. D., 1990, “A New Wide Range Equation of State for Helium,” *Adv. Cryog. Eng.*, **35**, pp. 1465–1475.
- [31] Arp, V. D., McCarty, R. D., and Friend, D. G., 1998, “Thermophysical Properties of Helium-4 from 0.8 to 1500 K with Pressures to 2000 MPa,” NIST Technical Note 1334, Boulder, CO.
- [32] Hands, B. A., and Arp, V. D., 1981, “A Correlation of Thermal Conductivity Data for Helium,” *Cryogenics*, **21**(12), pp. 697–703.
- [33] Lambert, J. D., 1977, *Vibrational and Rotational Relaxation in Gases*, Oxford University Press, Oxford.
- [34] Kruger, C. H., and Walter, G. V., 1965, *Introduction to Physical Gas Dynamics*, John Wiley & Sons, Inc., New York.
- [35] Anderson, D. A., Tannehill, J. C., and Pletcher, R. H., 1984, *Computational Fluid Mechanics and Heat Transfer*, Hemisphere Publishing Corporation, New York.
- [36] Buelow, P., Venkateswaran, S., and Merkle, C. L., 1994, “The Effect of Grid Aspect Ratio on Convergence,” *AIAA J.*, **32**, pp. 2401–2406.
- [37] Feng, J., and Merkle, C. L., 1990, “Evaluation of Preconditioning Methods for Time Marching Systems,” AIAA paper no. 90-0016, AIAA 28th Aerospace Sciences Meeting, Reno, NV.
- [38] Buelow, P. E. O., 1995, “Convergence Enhancement of Euler and Navier-Stokes Algorithms,” Ph.D. thesis, Department of Mechanical Engineering, The Pennsylvania State University, University Park, PA.
- [39] DuChateau, P., and Zachmann, D., 1989, “Applied Partial Differential Equations,” Harper and Row Publishers, Inc., New York.
- [40] Edwards, C. H., and Penny, D. E., 1989, “Elementary Differential Equations With Boundary Value Problems,” Prentice-Hall, Inc., Englewood, NJ.